



# Fusion of GNSS and InSAR time series using the improved STRE model: applications to the San Francisco Bay Area and Southern California

Huineng Yan<sup>1</sup> · Wujiao Dai<sup>1</sup> · Lei Xie<sup>1,2</sup> · Wenbin Xu<sup>1</sup>

Received: 5 August 2021 / Accepted: 7 June 2022 / Published online: 5 July 2022  
© Springer-Verlag GmbH Germany, part of Springer Nature 2022

## Abstract

The spatio-temporal random effects (STRE) model is a classic dynamic filtering model, which can be used to fuse GNSS and InSAR deformation data. The STRE model uses a certain time span of high spatial resolution Interferometric Synthetic Aperture Radar (InSAR) time series data to establish a spatial model and then obtain a deformation result with high spatio-temporal resolution through the state transition equation recursively in time domain. Combined with the Kalman filter, the STRE model is continuously updated and modified in time domain to obtain higher accuracy result. However, it relies heavily on the prior information and personal experience to establish an accurate spatial model. To the authors' knowledge, there are no publications which use the STRE model with multiple sets of different deformation monitoring data to verify its applicability and reliability. Here, we propose an improved STRE model to automatically establish accurate spatial model to improve the STRE model, then apply it to the fusion of GNSS and InSAR deformation data in the San Francisco Bay Area covering approximately 6000 km<sup>2</sup> and in Southern California covering approximately 100,000 km<sup>2</sup>. Our experimental results show that the improved STRE model can achieve good fusion effects in both study areas. For internal inspection, the average error RMS values in the two regions are 0.13 mm and 0.06 mm for InSAR and 2.4 and 2.8 mm for GNSS, respectively; for Jackknife cross-validation, the average error RMS values are 6.0 and 1.3 mm for InSAR and 4.3 and 4.8 mm for GNSS in the two regions, respectively. We find that the deformation rate calculated from the fusion results is highly consistent with the existing studies, the significant difference in the deformation rate on both sides of the major faults in the two regions can be clearly seen, and the area with abnormal deformation rate corresponds well to the actual situation. These results indicate that the improved STRE model can reduce the reliance on prior information and personal experience, realize the effective fusion of GNSS and InSAR deformation data in different regions, and also has the advantages of high accuracy and strong applicability.

**Keywords** Deformation · Spatio-temporal random effects model · Data fusion · GNSS · InSAR time series · High spatio-temporal resolution

## 1 Introduction

With the development of GNSS and InSAR technology, extensive applications have been applied in the field of geodetic surveying, especially in deformation monitoring and disaster awareness (Xu et al. 2018; Carlà et al. 2019).

Because GNSS is a point-oriented technology, limited by deployment cost and the difficulty of installing instruments and equipment, it is difficult to ensure that the spatial density can meet the research needs, and the monitoring accuracy will be affected by the site layout methods (such as deeply founded sites and sites mounted to a building) and the external environment. Although the spatial resolution of InSAR is high enough for large-scale monitoring, the temporal resolution is limited by the satellite revisit period, and the accuracy is affected by atmosphere (Yu et al. 2020; Xiao et al. 2021), decorrelation effect, orbital error, and other data processing errors (Cao et al. 2018). Therefore, in some deformation monitoring and disaster awareness scenarios, it is difficult for us

✉ Wenbin Xu  
wenbin.xu@csu.edu.cn

<sup>1</sup> School of Geosciences and Info-Physics, Central South University, Changsha 410083, Hunan, China

<sup>2</sup> Department of Land Surveying and Geo-Informatics, The Hong Kong Polytechnic University, Kowloon, Hong Kong, China

to obtain accurate deformation information through a standalone monitoring technique. In this case, combining GNSS and InSAR data can better provide high spatio-temporal resolution and precision deformation result, thus providing a richer data source for geophysical inversion and assisting us to obtain more reliable inversion results (Bekaert et al. 2016; Xu et al. 2016; Wan et al. 2018; Aslan et al. 2019).

According to the fusion mode, GNSS and InSAR data fusion can be divided into four categories:

- 1) The observation equation is established based on the common physical quantities reflected by different deformation data. Walters et al. (2014) constructed the equations of GPS and InSAR with spherical triangle vertex velocity based on the same strain rate assumption, and solved by weighted least squares inversion; Fuhrmann et al. (2015) obtained the linear velocity from single InSAR, leveling, and GNSS data, then used ordinary Kriging interpolation and least squares adjustment to calculate the combined velocity field.
- 2) The difference between the displacement values of different observation methods is modeled and corrected. Farolfi et al. (2018) interpolated the offset calibration between GNSS permanent site and InSAR PSI data with multilevel B-spline model; Neely et al. (2019) fitted the difference between the GNSS and InSAR displacement data through second-order polynomial surface.
- 3) By constructing optimization equations that integrate multi-source observation data, the parameter solving is transformed into an equation optimization problem. Hu et al. (2011) combined the Gibbs energy function and BFGS method, derived three-dimensional ground motions from the fusion of InSAR and GPS measurements; Ji et al. (2020) used Markov random field-based L1 regularization to reconstruct the Gibbs energy equation, and differential evolution algorithm is used to minimize the energy function to derive the ground motion.
- 4) The spatio-temporal dynamic model is used to describe the evolution of the displacement fields, and the high spatio-temporal resolution displacement result can be obtained. Liu et al. (2018) proposed fusing InSAR and GNSS data based on the spatio-temporal random effects (STRE) model, the fusion result is obtained by the spatial model and recurring its state transition equation in time domain; Shi et al. (2019) proposed an enhanced STRE (eSTRE) fusion method, which considers spatial heterogeneity in spatial modeling.

Since the fourth method can directly fuse multi-source displacement data and does not need to construct a function between the deformation observation and the physical quantity (this may have deviations), we apply in-depth research

to further improve this approach. As a classic dynamic filtering model in the fourth method, the STRE model (Cressie et al. 2010; Katzfuss and Cressie 2011) has the advantages of dimensionality reduction and avoids storing and reversing super-large matrices.

For the current research on fusion of GNSS and InSAR deformation data using the STRE model, Liu et al. (2018) used the layers quadtree approach to uniformly select the spatial basis at multiple scales, but they did not explain how to determine the range at each scale, which highly depends on personal data processing experience and operational skills; Shi et al. (2019) proposed eSTRE model based on Liu's work (using the same set of data which covers an area of approximately  $120 \times 130$  km and includes only 15 periods of InSAR data), which considers spatial heterogeneity and improves the accuracy of spatial modeling by adding spatial basis in the local heterogeneous region, but it depends more on the prior knowledge of the study area.

In summary, there are still some deficiencies in the current research of using STRE model to fuse GNSS and InSAR deformation data. First, Liu et al. (2018) and Shi et al. (2019) only used a set of deformation observation data, which is insufficient with the current InSAR time series data, for example, the data of Sentinel-1 satellites can reach at least 12-days temporal resolution and covers large spatial areas (250 km swath width in interferometric mode) in most areas of the Earth's surface. Because the spatio-temporal behavior of the denser deformation signals in a larger area is expected to be more complicated, even with a mixture of instantaneous and latency deformation components, these deformations manifest in linear and nonlinear forms (Fukuda and Johnson 2010; Minson et al. 2014). Secondly, their fusion method strongly relies on prior information and personal experience, which severely hinders the application and promotion of the STRE model in the data fusion.

To solve these two problems and improve the applicability of the STRE model, here we propose an improved STRE model and apply it to fuse GNSS and InSAR observation data in a small area (approximately  $70 \times 95$  km) and a large area (approximately  $285 \times 380$  km) to verify the effectiveness of the model.

## 2 Improved STRE model

Based on the existing STRE model for GNSS and InSAR data fusion, we propose an improved STRE model, which optimizes the spatial modeling process through the method of spatial basis automatic selection, to reduce the dependence on prior information and personal experience. Furthermore, we improve the applicability and stability of STRE model in the process of GNSS and InSAR data fusion.

The basic principle of the STRE model is to construct the spatio-temporal Kalman observation equation based on the spatial model, different from pure spatial interpolation methods such as kriging interpolation (Cressie 1990), which weight the observations of the specific neighborhood of the unknown point to predict the optimal value.

The STRE model (Cressie and Johannesson 2008) decomposes the spatio-temporal observation data  $Z(s, t)$  into the trend term  $\mu_t(s)$ , which represents the change trend of data in the time domain, local variation  $v(s, t)$  describing the obvious large-scale numerical aggregation in the spatial domain which mainly includes the overall change information of the data block, subtle variation  $\xi(s, t)$  depicting small-scale numerical changes that are relatively discrete in the spatial domain and supplements the information missed by local variation, and observation noise  $\epsilon_t(s)$  caused by external environment and data calculation, so that the model results are closer to the modeled data without being too smooth.

$$Z(s, t) = \mu_t(s) + v(s, t) + \xi(s, t) + \epsilon_t(s) \quad (1)$$

where  $\mu_t(s)$  is obtained by taking the mean value of the observations in the spatial domain,  $v(s, t)$  is calculated by spatial modeling,  $\xi(s, t)$  is estimated by the expectation–maximization (EM) iteration combined with the fixed rank forward filter (FRF) or fixed rank backward smoothing (FRS), and  $\epsilon_t(s)$  can be regarded as a Gaussian white noise process.

The process of fusing GNSS and InSAR data using the improved STRE model can be divided into five steps (as shown in Fig. S1 in the Supplementary Material). First, the GNSS and InSAR displacement data are obtained, and the measurement geometry is unified. Next, the InSAR data are used for spatial modeling. Then, the spherical model is used to separate the variances of subtle variation and observation noise. Subsequently, the GNSS weight is estimated by the variance component estimation (Harville 1977). Finally, the FRF and FRS of the EM iteration are carried to obtain the time-varying state argument and small-scale subtle variation, until the termination condition is met, and the deformation fusion results can be calculated according to Eq. (1). The details are as follows:

## 2.1 Unified measurement geometry

First, the measurement geometry of GNSS and InSAR data needs to be unified. Here we project the GNSS three-dimensional deformation ( $Z_n, Z_e, Z_u$ ) to the InSAR line of sight (LOS) direction ( $Z_l$ ) through the azimuth of the satellite heading vector  $\alpha$  (positive clockwise from the North) and the radar incidence angle  $\theta$  at the target point (Fialko et al. 2001):

$$Z_l = Z_n \sin(\alpha) \sin(\theta) - Z_e \cos(\alpha) \sin(\theta) + Z_u \cos(\theta) \quad (2)$$

If multi-geometry InSAR data either from different SAR space crafts or the two-track observations (ascending and descending) are available in the same study area and time duration, we can also unify the measurement geometry of GNSS and InSAR data according to Eq. (2), to obtain the GNSS deformation in the LOS direction of the InSAR satellite. By fusing each group of InSAR displacement time series with GNSS data, we can obtain the fusion result with high spatio-temporal resolution corresponding to each group of InSAR data. The research of Fuhrmann and Garthwaite (2019) shows that combined with the relationship between the observation values in E, N, U and the LOS direction, multiple InSAR data or other independent geodetic data can be used to decompose the E, N, U components directly through the least square adjustment. Therefore, in combination with multi-track and multi-platform InSAR data, it is possible to obtain three-dimensional high spatio-temporal resolution deformation result through data fusion.

After the direction of the observation data is unified, we adopted a single GNSS site as a reference point for measurement geometry connection (Chaussard et al. 2014; Mahapatra et al. 2018), because this method is simple to implement and can be validated by unconnected GNSS sites in the study area (Johnston et al. 2021). For an optimal selection of a GNSS site as reference site, we consider the amount of missing data within the time range of InSAR observations, the stability of the GNSS site and the difference between GNSS and InSAR data after the measurement geometry is unified.

The difference between the GNSS and InSAR data after the unification of the framework is small, which is manifested as a spatially uncorrelated error. According to the Sect. 2.3 "Separate the subtle variation and noise", the error caused by the GNSS reference site can be added into the observation noise, so the error caused by the GNSS reference site has less effect on the subtle variation  $\xi(s, t)$ . In addition, since GNSS data can largely reduce the effects of atmospheric errors by differencing between GNSS sites, unifying the InSAR and GNSS data can help mitigate the effects of undesirable turbulence in InSAR time series data.

## 2.2 InSAR data spatial modeling

After the measurement geometry is unified, we perform spatial modeling on the InSAR data. The spatial model expresses the local variation  $v(s, t)$  as the product of the spatial basis  $S_t(s)$  and the time-varying state argument  $a(t)$ :

$$v(s, t) = S_t(s)a(t) \quad (3)$$

where  $S_t(s) = [S_{1,t}(s), S_{2,t}(s), \dots, S_{r,t}(s)]'$  is used to describe the degree of spatial correlation between the spatial basis and surrounding sites,  $a(t) = [a_1(t), a_2(t), \dots, a_r(t)]'$  is used to describe

the temporal change of the response value corresponding to the spatial basis.

Although in theory, the value of  $S_t(s)$  is temporally and spatially correlated. To realize the construction and solution of the spatial model, we simplify  $S_t(s)$  to be uncorrelated in the temporal domain. This simplification will cause the error of spatial modeling to gradually increase over time. By estimating subtle variation  $\xi(s, t)$ , we can well supplement the deformation information missed by spatial modeling.

During the experiment, we choose the bi-square function (Cressie and Johannesson 2008) as the basis function to calculate  $S_t(s)$ :

$$S(s) = \begin{cases} \{1 - (s - c_l/g_l)^2\}^2 & s - c_l < g_l \\ 0 & \text{otherwise} \end{cases} \quad (4)$$

where  $s$  is the location of InSAR pixel,  $c_l$  is the location of  $l$  th scale spatial basis,  $\|s - c_l\|$  is the distance between the InSAR pixel and the spatial basis,  $g_l$  is the distance threshold.

After constructing the spatial basis  $S_t(s)$ , the estimation of the time-varying state argument  $\hat{\alpha}(t)$  and residual  $V_t$  can be obtained through the least squares. The calculation formula is as follows:

$$\hat{\alpha}(t) = (S'S)^{-1}S'(\mathbf{Z}_t - \boldsymbol{\mu}_t) \quad (5)$$

$$V_t = \mathbf{Z}_t - \boldsymbol{\mu}_t - S[(S'S)^{-1}S'(\mathbf{Z}_t - \boldsymbol{\mu}_t)] \quad (6)$$

## 2.2.1 Spatial bases selection method

The spatial bases selection is an important part of spatial modeling. A suitable selection scheme can ensure that sufficient local deformation is obtained, however, there is no reference criterion to assist the spatial bases selection. Interestingly, during the data fusion experiment, we found that in the initial stage, the model effect was basically proportional to the number of spatial bases; but when increased to a certain level, the effect peaked. After this peak, if the number increased, the effect would not be significantly improved, and overfitting may even occur.

In fact, the spatial bases selection is mainly determined by the calculation amount and accuracy. The calculation amount can be measured by the number of spatial bases, the accuracy can be judged by the error RMS value. Based on this, we propose an exact selection criterion  $Ind_s$ :

$$Ind_s = V_{RMS}/V_N = (RMS_1 - RMS_2)/(N_1 - N_2) \quad (7)$$

where  $V_{RMS}$  is the difference in the error RMS value between the two selection schemes and  $V_N$  is the difference in the number of spatial bases.  $Ind_s$  characterizes the degree to

which increasing the number of spatial bases can improve the accuracy of spatial modeling. What we need to do is to find the most suitable selection scheme according to the criterion  $Ind_s$ .

To reduce the dependence on prior information and capture more local deformation, spatial bases are evenly distributed and performed on multiple scales until the residual stabilizes (Cressie and Johannesson 2008). The details are shown in Fig. S2 in the Supplementary Material.

In the improved STRE model, the spatial bases selection mainly includes the following steps:

- 1) Select a large range value and calculate the spatial modeling residual.
- 2) A series of continuous range values are obtained by gradually reducing the range value.
- 3) For each range value, perform spatial modeling and calculate the error RMS value.
- 4) Group according to the number of spatial bases and select the range value with the smallest error RMS value as the representative.
- 5) The  $Ind_s$  corresponding to each group is calculated and the median value is obtained.
- 6) Finally, the last spatial bases selection scheme whose criterion value is greater than the median value is selected as the optimal selection scheme.

Although the spatial bases selection method requires multiple spatial modeling and residual calculation, each calculation only needs to perform a least squares operation (Eqs. 5 and 6) for the InSAR data, so the calculation amount will not be significantly increased.

## 2.3 Separation of subtle variation and noise

In the residual of InSAR data spatial modeling calculated by Eq. (6), there is still some deformation information that the spatial model did not capture, including subtle variation  $\xi(s, t)$  and observation noise  $\epsilon_t(s)$ . To model the residuals of the spatial model, the subtle variation  $\xi(s, t)$  and the observation noise  $\epsilon_t(s)$  are modeled as temporally and spatially uncorrelated Gaussian white noise ( $\xi(s_i, t) \sim N(0, \sigma_{\xi, s_i}^2)$ ,  $\epsilon_t(s_i) \sim N(0, \sigma_{\epsilon, s_i}^2)$ ).

Since the differences between the InSAR and GNSS data after the unified measurement geometry do not show significant spatial clustering, we consider the variance of the observation noise  $\epsilon_t(s)$  to be spatially uncorrelated. And the small-scale subtle variation is affected by the ability of spatial modeling to capture deformation information, so we consider that the variance of the subtle variation  $\xi(s, t)$  is spatially correlated. Based on these assumptions that the variances of  $\xi(s, t)$  and  $\epsilon_t(s)$  have different spatial distribution patterns,

we compute the semi-variogram residual value  $\gamma$  and fit it with a spherical model to separate the variances of  $\xi(s, t)$  and  $\epsilon_t(s)$ :

$$\gamma(h) = \frac{1}{2N} \sum_{i=1}^N [V_t(x_i) - V_t(x_i + h)]^2 \quad (8)$$

$$\gamma(h) = \begin{cases} 0 & h = 0 \\ C_0 + C \left( \frac{3h}{2a} - \frac{h^3}{2a^3} \right) & 0 < h \leq a \\ C_0 + C & h > a \end{cases} \quad (9)$$

where  $h$  is the distance between different InSAR pixels,  $N$  is the number of InSAR pixels,  $V_t$  is the spatial modeling residual,  $x_i$  is the location of InSAR pixel,  $a$  is the variable range,  $C_0$  is the nugget value which represents the variance of the observation noise, and  $C$  is the sill value which represents the variance of subtle variation.

After obtaining the variance of the subtle variation  $\xi(s, t)$  corresponding to each period of InSAR observation data, we use the temporal interpolation method to calculate the variance of  $\xi(s, t)$  corresponding to each observation moment.

## 2.4 Estimation of GNSS accuracy

Following our distributional assumptions for subtle variation and observational noise, the residuals from spatial modeling of InSAR data ( $d_t^{ins}$ ) and GNSS data ( $d_t^{gnss}$ ) obey the following distributions:

$$\begin{pmatrix} d_t^{ins} \\ d_t^{gnss} \end{pmatrix} \sim N \left[ 0, \begin{pmatrix} \sigma_\xi^2 I_{ins} + \sigma_{ins}^2 I_{ins} & 0 \\ 0 & \sigma_\xi^2 I_{gnss} + \sigma_{gnss}^2 I_{gnss} \end{pmatrix} \right] \quad (10)$$

To determine the accuracy of the GNSS observation data, we first obtain the weight of the InSAR residual  $d_t^{ins}$  compared to the GNSS residual  $d_t^{gnss}$  through the variance component iterative estimation (Harville 1977; Xu et al. 2007). Since we have calculated the InSAR observation noise variance  $\sigma_{ins}^2$  and the subtle variation variance  $\sigma_\xi^2$  in Sect. 2.3, combined with the weight of the InSAR residual  $d_t^{ins}$  compared to the GNSS residual  $d_t^{gnss}$  and Eq. (10), we can calculate the GNSS observation noise variance  $\sigma_{gnss}^2$  to determine the accuracy of the GNSS data relative to the InSAR data.

## 2.5 EM iterative estimation

Until this step, we have obtained the trend term  $\mu_t(s)$ , the spatial basis  $S$ , the time-varying state quantity  $\hat{a}(t)$  corresponding to the InSAR data, the variance of the subtle

variation  $\sigma_\xi^2$ , the variance of GNSS observation noise  $\sigma_{gnss}^2$  and InSAR observation noise  $\sigma_{ins}^2$ .

To obtain the deformation value at each observation moment, we estimate the spatio-temporal Kalman's state transition matrix  $\Phi$  and the system noise covariance matrix  $Q$  based on EM iteration (Katzfuss and Cressie 2011) using GNSS data and InSAR data, and the data processing formula is as follows:

Observation model:

$$\begin{aligned} \begin{pmatrix} Z_t^{ins} \\ Z_t^{gnss} \end{pmatrix} &= \begin{pmatrix} \mu_t^{ins} \\ \mu_t^{gnss} \end{pmatrix} + \begin{pmatrix} S_{ins} \\ S_{gnss} \end{pmatrix} \alpha(t) \\ &\quad + \begin{pmatrix} \xi_t^{ins} \\ \xi_t^{gnss} \end{pmatrix} + \begin{pmatrix} \epsilon_t^{ins} \\ \epsilon_t^{gnss} \end{pmatrix} \\ &= \begin{pmatrix} \mu_t^{ins} \\ \mu_t^{gnss} \end{pmatrix} + \begin{pmatrix} S_{ins} \\ S_{gnss} \end{pmatrix} \alpha(t) + \begin{pmatrix} d_t^{ins} \\ d_t^{gnss} \end{pmatrix} \end{aligned} \quad (11)$$

The spatial modeling residuals distribution of GNSS and InSAR data follows Eq. (10).

State transition equation:

$$\alpha(t) = \Phi \alpha(t-1) + \eta(t) \quad \eta(t) \sim N(0, Q) \quad (12)$$

where  $\alpha(t)$  is the time-varying state argument of the current time,  $\alpha(t-1)$  is the time-varying state argument of the previous time,  $\Phi$  is the state transition matrix,  $Q$  is the system noise covariance matrix.

Based on these formulas, the FRF and FRS of the EM iteration estimation (Shumway and Stoffer 1982) are used to calculate the time-varying state argument  $\alpha(t)$  and small-scale subtle variation  $\xi_t$  at each observation moment. The detailed formulas are shown in Sects. 2.5.1 and 2.5.2.

### 2.5.1 Fixed rank forward filter

One-step forecast and covariance matrix:

$$\hat{\alpha}_t^{t-1} = \Phi \hat{\alpha}_{t-1}^{t-1} \quad (13)$$

$$P_t^{t-1} = \Phi P_{t-1}^{t-1} \Phi' + Q \quad (14)$$

Gain matrix:

$$G_t = P_t^{t-1} S' \left( S P_t^{t-1} S' + D \right)^{-1} \quad (15)$$

where,  $D$  is the variance of spatial modeling residuals between InSAR and GNSS.

The filter state-argument  $\hat{a}_t^t$  and its covariance estimate  $P_t^t$ , the subtle variation  $\hat{\xi}_t^t$ :

$$\hat{a}_t^t = \hat{a}_t^{t-1} + G_t (Z_t - \mu_t - S \hat{a}_t^{t-1}) \quad (16)$$

$$\mathbf{P}_t^t = \mathbf{P}_t^{t-1} - \mathbf{G}_t S \mathbf{P}_t^{t-1} \quad (17)$$

$$\hat{\xi}_t^t = \sigma_{\xi}^2 (\mathbf{S} \mathbf{P}_t^{t-1} \mathbf{S}' + \mathbf{D})^{-1} (\mathbf{Z}_t - \boldsymbol{\mu}_t - S \hat{\mathbf{a}}_t^{t-1}) \quad (18)$$

The cross-covariance matrix of  $\hat{\mathbf{a}}_{t-1}^{t-1}$  and  $\hat{\mathbf{a}}_t^t$ :

$$\mathbf{P}_{t|t-1}^t = \Phi \mathbf{P}_{t-1}^{t-1} - \mathbf{G}_t S \Phi \mathbf{P}_{t-1}^{t-1} \quad (19)$$

Posterior estimates of  $\Phi$  and  $\mathbf{Q}$ :

$$\Phi = \mathbf{B}_1 \mathbf{A}_1^{-1} \quad (20)$$

$$\mathbf{Q} = \frac{\mathbf{C}_1 - \mathbf{B}_1 \mathbf{A}_1^{-1} \mathbf{B}_1'}{T} \quad (21)$$

where,  $\mathbf{A}_1 = \sum_{t=1}^T \mathbf{P}_{t-1}^{t-1} + \hat{\mathbf{a}}_{t-1}^{t-1} \hat{\mathbf{a}}_{t-1}^{t-1'}$ ,  $\mathbf{B}_1 = \sum_{t=1}^T \mathbf{P}_{t|t-1}^{t-1} \hat{\mathbf{a}}_t^t \hat{\mathbf{a}}_{t-1}^{t-1'}$ ,  $\mathbf{C}_1 = \sum_{t=1}^T \mathbf{P}_t^t + \hat{\mathbf{a}}_t^t \hat{\mathbf{a}}_t^t'$ .

First, we give the initial values of the state transition matrix  $\Phi$ , the time-varying state-argument  $\hat{\mathbf{a}}_{0|0}$  and the weight matrix  $\mathbf{P}_{0|0}$  at the first moment. Then, by continuously updating the calculation Eqs. (13) to (19), the time-varying state-argument  $\hat{\mathbf{a}}_t^t$ , subtle variation  $\hat{\xi}_t^t$ , weight matrix  $\mathbf{P}_t^t$  and cross covariance matrix  $\mathbf{P}_{t|t-1}^t$  at each observation moment are obtained. After these calculations are completed, the posterior estimates of  $\Phi$  and  $\mathbf{Q}$  corresponding to FRF can be calculated by Eqs. (20) and (21), and then the new estimates of  $\hat{\mathbf{a}}_t^t$ ,  $\hat{\xi}_t^t$ ,  $\mathbf{P}_t^t$  and  $\mathbf{P}_{t|t-1}^t$  at each observation moment can be obtained by re-iterating Eqs. (13) to (19).

## 2.5.2 Fixed Rank backward Smooth

After FRF is completed, each calculated parameter ( $\hat{\mathbf{a}}_t^t$ ,  $\hat{\xi}_t^t$ ,  $\mathbf{P}_t^t$ ,  $\mathbf{P}_{t|t-1}^t$ ) is substituted into the FRS backward smoothing, to obtain the FRS smoothing subtle variation  $\hat{\xi}_t^T$ , time-varying state-argument  $\hat{\mathbf{a}}_t^T$ , weight matrix  $\mathbf{P}_t^T$  at each observation moment.

Gain matrix:

$$\mathbf{J}_t = \mathbf{P}_{t-1}^{t-1} \Phi' (\mathbf{P}_t^{t-1})^{-1} \quad (22)$$

The smoothing state-argument  $\hat{\mathbf{a}}_t^T$  and its covariance estimate  $\mathbf{P}_t^T$ , the subtle variation  $\hat{\xi}_t^T$ :

$$\hat{\mathbf{a}}_t^T = \hat{\mathbf{a}}_t^t + \mathbf{J}_t (\hat{\mathbf{a}}_{t+1}^T - \hat{\mathbf{a}}_t^{t-1}) \quad (23)$$

$$\mathbf{P}_t^T = \mathbf{P}_t^t + \mathbf{J}_t (\mathbf{P}_{t+1}^T - \mathbf{P}_t^{t-1}) \mathbf{J}_t' \quad (24)$$

$$\hat{\xi}_t^T = \hat{\xi}_t^t - \sigma_{\xi}^2 \mathbf{G}_t' \Phi (\mathbf{P}_{t+1}^t)^{-1} (\hat{\mathbf{a}}_{t+1}^T - \hat{\mathbf{a}}_{t+1}^t) \quad (25)$$

The cross-covariance matrix of  $\hat{\mathbf{a}}_t^T$  and  $\hat{\mathbf{a}}_{t+1}^T$ :

$$\mathbf{P}_{t+1|t}^T = \mathbf{P}_{t+1}^{t+1} \mathbf{J}_t' + \mathbf{J}_{t+1} (\mathbf{P}_{t+2|t+1}^T - \Phi \mathbf{P}_{t+1}^{t+1}) \mathbf{J}_t' \quad (26)$$

Substituting the corresponding variables into Eqs. (20) and (21), the posterior estimates of  $\Phi$  and  $\mathbf{Q}$  corresponding to FRS can be calculated.

Using the newly estimated posterior parameters  $\Phi$  and  $\mathbf{Q}$ , FRF and FRS are performed again, and the process is repeated until the iteration termination condition is satisfied (Liu et al. 2018). Finally,  $\mathbf{a}(t)$  and  $\xi_t$  obtained by FRF and FRS are substituted into Eq. (11), to calculate the filtering and smoothing estimates. In the fusion experiment, we used smoothing estimates as the result.

## 3 Deformation data fusion experiment

We use the improved STRE model to fuse the GNSS and InSAR displacement data of the San Francisco Bay Area and Southern California. To verify the fusion effect, we first used all the GNSS and InSAR data to model and verify the accuracy and internal reliability, then verify the accuracy and external reliability by jackknife cross-validation (Miller 1974).

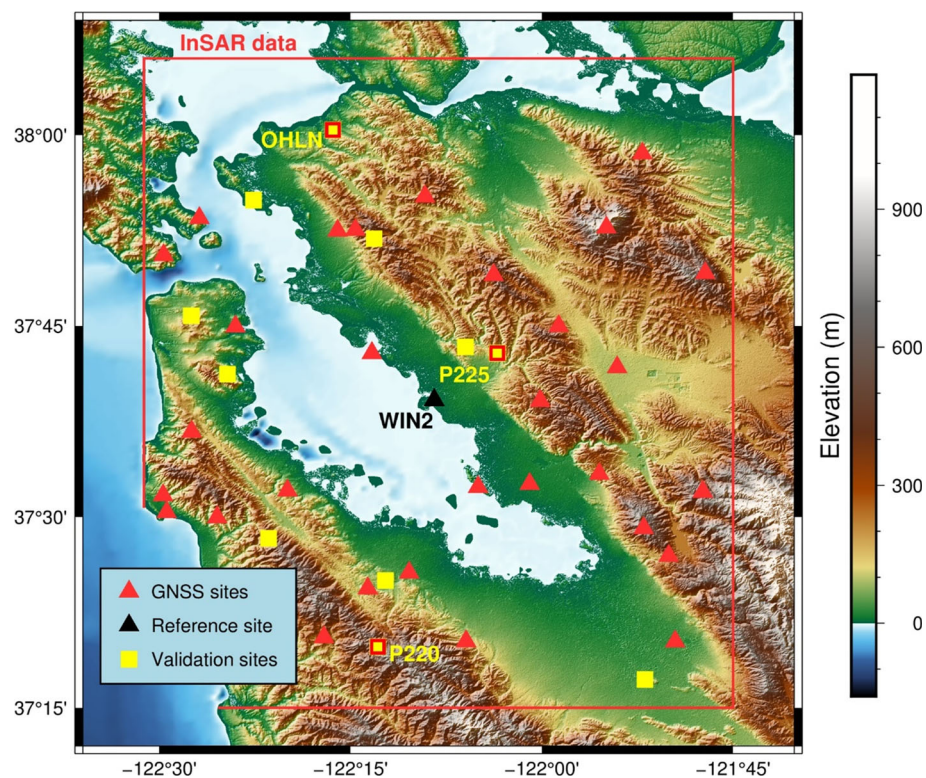
### 3.1 The San Francisco Bay Area

#### 3.1.1 GNSS and InSAR data processing

The first study area is the San Francisco Bay Area, which is approximately  $70 \times 95$  km (Fig. 1). The standardized interferogram products of Sentinel-1A/B obtained by ARIA (<https://aria.jpl.nasa.gov/products>) were used to generate InSAR displacement time series data from 2015-06-05 to 2019-07-02 (i.e., 35 epochs). We used the MintPy software (Zhang et al. 2019) to estimate the InSAR time series. The ERA-5 atmospheric model (Jolivet et al. 2011, 2014) were used to correct the tropospheric delay, and the DEM residual term was estimated in the time domain (Fattah and Amelung 2013). The date of each period of InSAR data is listed in Table S1 in the Supplementary Material. Some data were not selected due to low interferometric coherence and large differences in the derived displacement values compared to the GNSS. The GNSS data under the IGS14 reference frame were downloaded from the Nevada Geodesy Laboratory (Blewitt et al. 2018), and 42 GNSS sites were selected.

First, we unified the measurement geometry of the GNSS and InSAR data. We repaired the step items and gross errors in the GNSS data according to the event record file and the deformation characteristic function, and then projected the GNSS displacement in the LOS direction. Considering

**Fig. 1** Spatial distribution of topography and GNSS sites in the San Francisco Bay Area. The red solid line is the InSAR data footprint. The squares and triangles denote GNSS site locations, squares represent the site used for Jackknife cross-validation, those with red frame show the results in the paper, and the others show the results in the Supplementary Material



that the ERA-5 atmospheric model may only be suitable for decreasing the long-wave atmospheric screen, the errors caused by localized water vapor may remain in the InSAR time series. But due to the favorable humidity, vegetation and landscape in the California area, the water vapour effects in the area of interest are generally small. Therefore, we unify the measurement geometry by selecting the GNSS reference site (see the penultimate paragraph of Sect. 2.1 for details). Based on the requirements for a suitable reference point discussed in Sect. 2.1, WIN2 was used as the reference site to unify the measurement geometry. We select 7 periods of InSAR displacement time series data after unified measurement geometry at equal intervals and plot them in row "a" of Fig. 2. The results of all 35 periods are shown in Fig. S3, and the displacement comparison of the GNSS sites and adjacent InSAR pixel is shown in Fig. S4 in the Supplementary Material.

As shown in row "a" of Fig. 2 and Fig. S3, the displacement of the San Francisco Bay Area mainly occurs in the southwest part and manifests as subsidence. From the comparison between the GNSS site and the adjacent InSAR pixels (Fig. S4 of the Supplementary Material), the GNSS and InSAR data after the measurement geometry unified are in good agreement, and the error RMS is about 3–6 mm.

After the measurement geometry was unified, we calculated the spatial average of the GNSS and InSAR data and used wavelet analysis to remove the noise (Fig. S5 of the

Supplementary Material), after which the trend term was removed from the GNSS and InSAR data.

### 3.1.2 InSAR data spatial modeling

We adopted the method in Sect. 2.2.1 to select spatial bases and calculate the error RMS value and criterion  $Ind_s$  (Fig. 3). In the end, the spatial bases we selected contained three different scales, the ranges of each scale were  $0.304^\circ$ ,  $0.152^\circ$ , and  $0.076^\circ$ , and the spatial bases numbers were 9, 30, and 110 (Fig. S6 in the Supplementary Material).

After the spatial bases are determined, the time-varying state argument of each period is obtained by least squares as described in Eq. (5), and the 7 periods spatial modeling results and residuals are shown in row "b" and "d" of Fig. 2, all 35 periods results and residuals are shown in Fig. S7 and S8 in the Supplementary Material.

As can be seen from row "b" of Fig. 2 and Fig. S7, the overall deformation trend can be obtained from the spatial modeling, but the deformation captured by the spatial bases is too smooth, and some obvious deformation details are omitted, especially in the southwest and east of the region.

From row "d" of Fig. 2 and Fig. S8, the error of the relatively gentle deformation area is small; however, in the area with relatively complicate deformation, there is still obvious deformation information in the residual. For the southwest corner, the error clustering is relatively serious, and some are close to 30 mm, indicating that the ability of the spatial

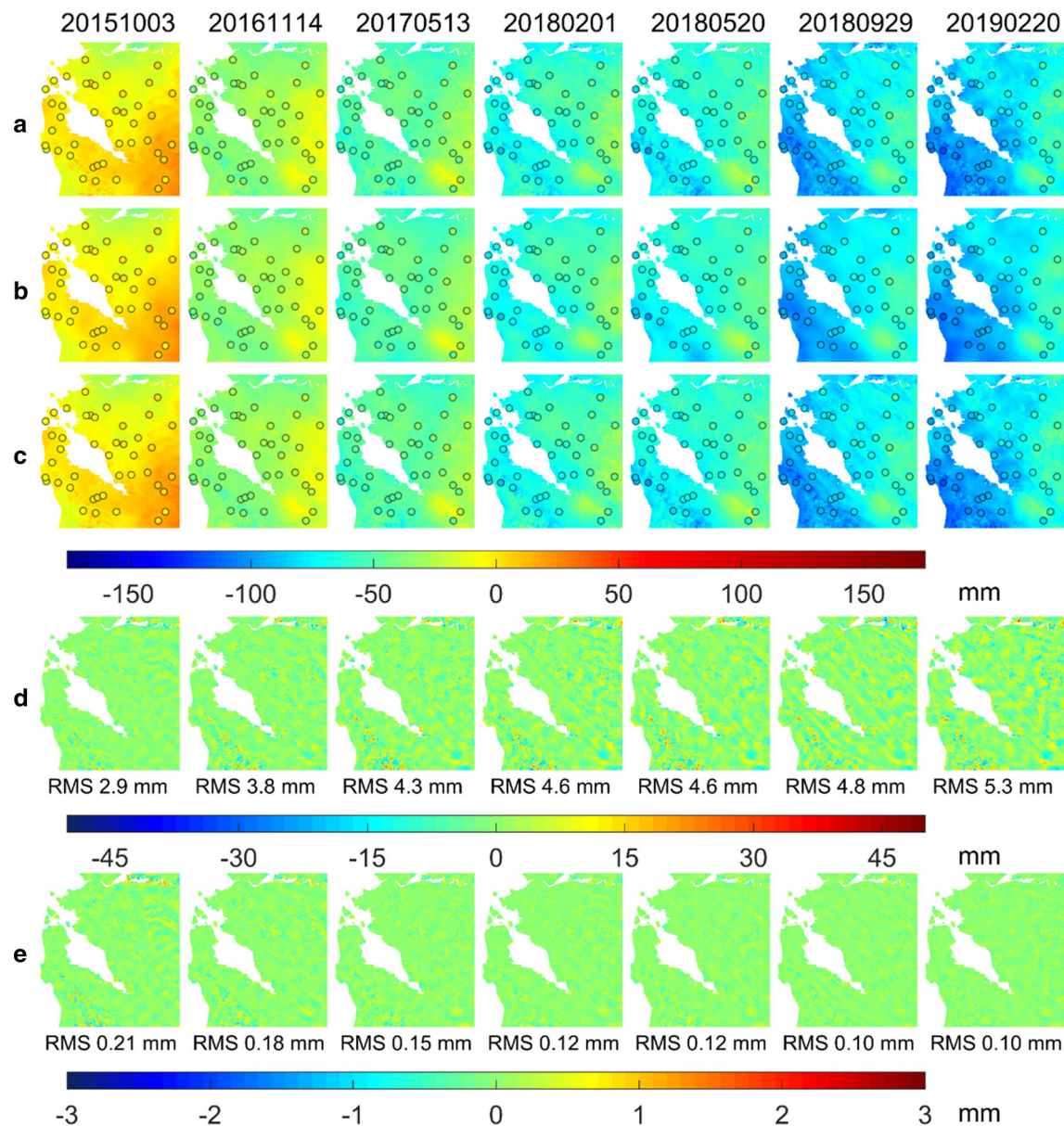


**Fig. 2** Combination diagram of 7 periods InSAR displacement time series data relative to 2015-06-05 in the San Francisco Bay Area. The rows "a", "b" and "c" respectively represent the InSAR data after measurement geometry unified, spatial modeling results and fusion results, the circle indicates the GNSS site locations, and the color indicates the

deformation value. The row "d" represents the residual of spatial modeling, and row "e" represents the residual of the fusion result. Warm colors (i.e., positive values) denote surface displacements toward the satellite, and cold colors (i.e., negative values) denote the away-motion from the satellite

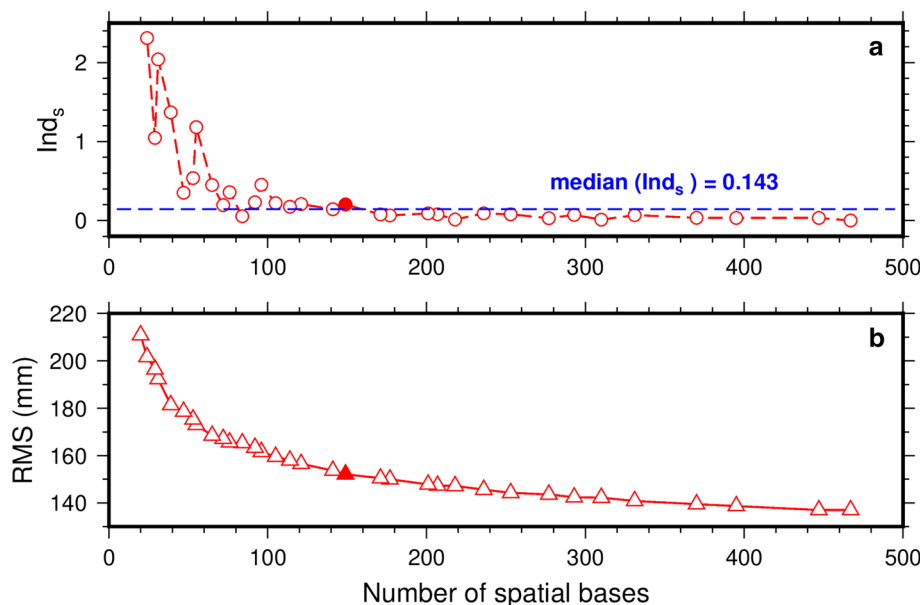
model to capture detailed deformation information is insufficient. Fig. S8 also shows that the error RMS values are all below 6 mm and show a gradual upward trend, which means that while the deformation situation becomes more complex over time, deformation missing from the spatial model gradually increases, which is determined by the characteristic that the spatial model is mainly used to reflect the overall spatial distribution characteristics.

### 3.1.3 GNSS and InSAR data fusion

We add GNSS data for fusion and obtain the time-varying state argument and subtle variation in FRF and FRS at each observation moment through EM iterative estimation. Finally, the FRS result after multiple iterations is used as the fusion result of the improved STRE model.

We selected the GNSS sites that had data throughout the whole InSAR measurement period (a total of 12 sites) to test

**Fig. 3** Criterion and error RMS value for spatial modeling using different spatial basis range in the San Francisco Bay Area. (a) The red hollow circle represents the criterion  $Ind_s$  of spatial modeling, the red filled circle represents the criterion finally selected, the blue dotted line represents the median criterion value. (b) The red hollow triangle represents the error RMS value of spatial modeling, the red filled triangle represents the error RMS value finally selected



the accuracy of the improved STRE model. The model fusion result and original displacement value of the 3 GNSS sites are plotted in the first column of Fig. 4, and the other 9 GNSS sites are shown in Fig. S9. For the InSAR data, the 7 periods model fusion results and residuals are shown in row "c" and "e" of Fig. 2, all 35 periods results and residuals are shown in Fig. S10 and S11 in the Supplementary Material.

The first column of Fig. 4 and Fig. S9 show that the improved STRE model at these 12 GNSS sites are in good agreement with the original GNSS displacement, and except for the SBRB site, the error RMS values are all less than 2.5 mm. The larger RMS values at site SBRB can be explained by significant fluctuations in the original data while the improved STRE model is relatively stable. This means that the improved STRE model not only reflects the overall displacement trend, but also has a good smoothing effect on the noisy GNSS displacement data.

From row "c" of Fig. 2 and Fig. S10, it can be seen that the result of the improved STRE model is closer to the InSAR displacement value, both reflects the overall deformation trend and supplements the subtle numerical deformation details missing from the spatial model, especially in the southwest and east part where the deformation details are complicated. In addition, it can be clearly seen from Fig. S10 that since 2018-07-31, the subsidence in the southwest part (San Francisco and San Mateo) has gradually increased, especially on the periphery, where the deformation is obvious, while the deformation in other regions gradually tends to be flat. During the entire InSAR monitoring period, the uplift rate in the east part was relatively small, and it gradually turned to subsidence in the later period.

As can be seen from row "e" of Fig. 2 and Fig. S11, throughout the study area, the errors in the improved STRE

model are very small and within 3 mm. In areas with obvious deformations, such as the southwest corner and the east part, no obvious large-scale aggregate deformation residual information was found, indicating that the improved STRE model has a strong ability to capture deformation details and accurately reflect the observed deformation value. On the other hand, the error RMS values are all distributed below 0.21 mm, and the RMS value shows a trend of gradually decreasing over time, indicating that while the modeling data is enriched, the displacement details captured by the model are increasing, and the fusion result gradually approaches the observed InSAR displacement value, which also proves that the improved STRE model has good spatial and temporal stability and reliability.

Based on the fusion results, the CSBAS method (Neely et al. 2019) is used to calculate the deformation rate field. We plot the calculated deformation rate in Fig. 5, and draw 4 fault profile lines at intermediate intervals, one of the profile lines and the selected 3 representative pixels are drawn together in Fig. 5, and the other 3 profile lines are drawn in Fig. S12 in the Supplementary Material.

The left part of Fig. 5 shows that the deformation pattern of the San Francisco Bay Area is very complicated, the rate values are all negative and the spatial distribution is complex, and the deformation rate difference on both sides of the fault can be clearly seen. In the northeast part, the deformation rate was relatively small, and the distribution was relatively uniform, basically between -10 and -20 mm/yr. In the central seaport region, the deformation rate was relatively uniform, largely approximately -25 mm/yr, several large rate regions on both sides of the bank were basically consistent with the location of the city, and there was an obviously lower rate aggregation in the southeast (Silver Creek fault). High

settlement rates were mainly confined to the southwestern coastal area, and the area near point 1 reached approximately  $-35$  mm/yr, which may be caused by Holocene age mud deposits in the bay and long-term compaction of artificial landfills (Kooi and De Vries 1998; Bürgmann et al. 2006).

The spatial distribution of the deformation velocities is essentially consistent with the vertical direction deformation results of Shirzaei et al. (2018), but the deformation rate calculated by us was much larger, because the result of Shirzaei et al. is the deformation rate in the vertical direction (not including horizontal displacements) referenced to the GNSS site LUTZ, and our result is the deformation rate in the LOS direction (including the deformation information in the three directions) referenced to the GNSS site WIN2. Furthermore, the time span Shirzaei et al. selected extends from 2007-07-13 to 2010-10-17, and they also noted that global climate change (i.e., accelerated ice sheet mass loss and more rapid and prolonged droughts leading to unprecedented aquifer overdrafts) and local land subsidence exacerbated the deformation. The deformation rate of the North San Andreas Fault calculated from our analysis is approximately 30 mm/yr, which is similar to the 34 mm/yr calculated by Field et al. (2014, 2015) through the weighted summation of four deformation models (i.e., a geologic model without tectonic constraints, and three models inverted from geologic, geodetic, and stress data, respectively).

The first three subgraphs of the right part of Fig. 5 show that the fusion results are in perfect agreement with the InSAR displacement, with RMS less than 1 mm. Moreover, the fusion result can reveal the continuous deformation in time domain, which is helpful for understanding the deformation evolution in the InSAR data gap, and for supplementing the areas without GNSS sites or where the GNSS spatial density is insufficient.

It can be clearly seen from the fourth subgraph on the right part of Fig. 5 that there is a significant difference in deformation rate on both sides of the fault, this is consistent with the fact that the velocity of crustal movement on both sides of the fault are different. For the Hayward fault and the Concord fault, the deformation rate difference can even reach about 5 mm/yr.

### 3.1.4 Jackknife cross-validation

We selected 3 GNSS sites (the second column of Fig. 4) and 5 periods InSAR data with the same interval (Fig. 6) for the display of a Jackknife cross-validation (select one of the GNSS or InSAR data in turn to not participate in the modeling, and compare the model fusion results with the original data) of modelled displacement results. The validation results of the other 9 GNSS sites are shown in Fig. S13, the validation results and residuals of all 34 periods InSAR data (since the displacement of the first period is the reference value and all

are zero, it did not participate in the validation) are shown in Fig. S14 and Fig. S15, and the error RMS values are listed in Table S2 in the Supplementary Material.

From the second column of Fig. 4 and Fig. S13, the validation results are basically the same as the original GNSS displacement. Except for the SBRB site whose RMS value is slightly larger (due to high noise), the RMS values of the sites are all less than 5 mm. These indicate that the improved STRE model can accurately reflect the overall displacement trend and capture the deformation details. However, without the support of the original GNSS data, the model validation results showed more fluctuations. In general, there were few such anomalies, which did not affect the accurate description of the displacement information.

It can be seen from Fig. 6 that the model results (the second column) can reflect the original InSAR displacement information (the first column) well, and there is no large overall deviation, although some deformation information is omitted. From the distribution of residuals (the third column), the error has a certain degree of clustering and randomness, and most values are less than 10 mm, indicating that the model has little deviation. But for 2019-07-02, the error RMS value reaches 9.3 mm, and some residuals are greater than 15 mm. Because 2019-07-02 is the last period of data, so the improved STRE model cannot obtain deformation information from the later data. The residual error histogram (the fourth column) shows that the error distribution is reasonably close to a normal distribution, and most values are concentrated within 5 mm, indicating that the improved STRE model has good stability and reliability.

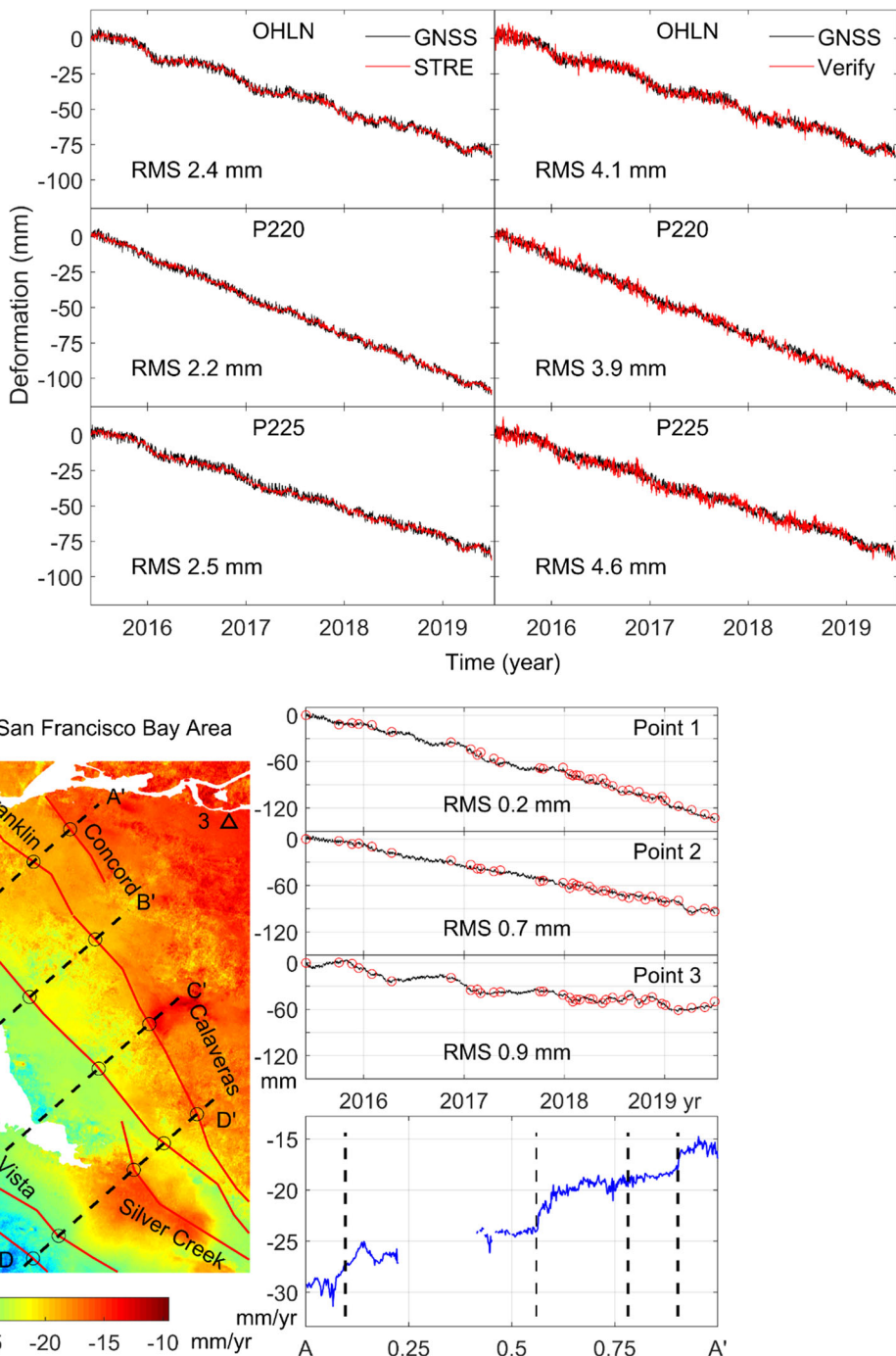
From Table S2, we can see that most of the error RMS values are around 6 mm, and only 3 periods of InSAR data are greater than 9 mm. This shows that even without the support of the original InSAR deformation data, the improved STRE model can basically predict the InSAR displacement value, and the obtained result does not have a large deviation from the original displacement. However, the RMS value of the validation results on some InSAR data is relatively large, this situation is related to the time interval of the InSAR data used.

## 3.2 Southern California

### 3.2.1 GNSS and InSAR data processing

The second study area is located in Southern California, approximately  $285 \times 380$  km (Fig. 7). We used InSAR time series included 73 periods from 2015-05-14 to 2019-05-17 from Xiaohua Xu, in which the GMTSAR software and a coherence-based SBAS method are applied (<https://topex.ucsd.edu/gmtsar/insargen/>, (Xu et al. 2017, 2021)). The specific acquisition dates are listed in Table S3 of the Supplementary Material. The GNSS data were downloaded

**Fig. 4** Combination diagram of displacement data in the LOS direction of 3 GNSS sites in the San Francisco Bay Area. The first column shows fusion results and original displacements, the second column shows Jackknife cross-validation result and original displacements. The red line is the result of the improved STRE model or Jackknife cross-validation, the black line is the original GNSS displacement



velocity map of the San Francisco Bay Area

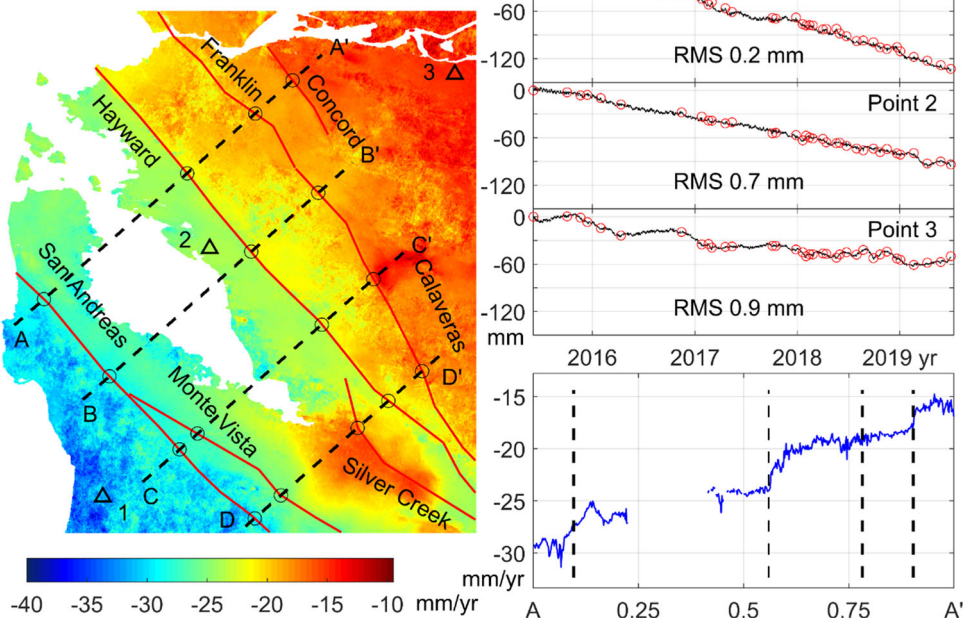


**Fig. 5** The deformation rate field in the LOS direction of the San Francisco Bay Area, the fusion results of 3 representative pixels and the velocity of the profile line A-A'. The figures on the left shows the deformation rate field, the triangles represent the InSAR pixel shown in the first three subgraphs on the right, the circle represents the intersection of the fault and the profile line (corresponding to the black dashed line in the fourth subgraph of the right figure), the black dashed line indicates

the location of the fault profile line, and the solid red lines indicate the locations of several major faults (Styron and Pagani 2020). For the figures on the right, the black line in the first three subgraphs represents the fusion result, and the circles represent the InSAR displacement value; the blue line in the fourth subgraph represents the deformation rate value on the profile line A-A', the number marked on the abscissa axis represents the length ratio on the profile line

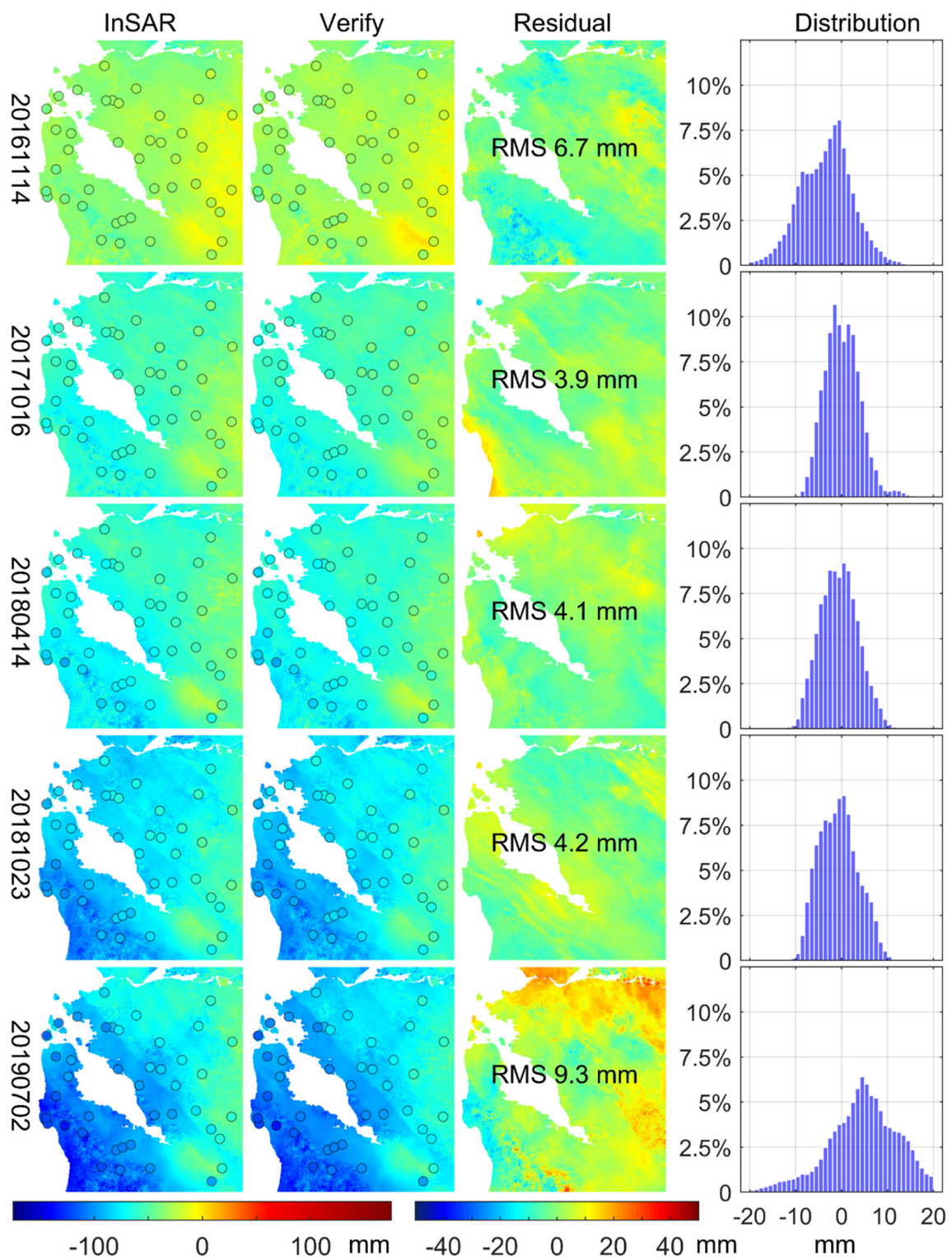
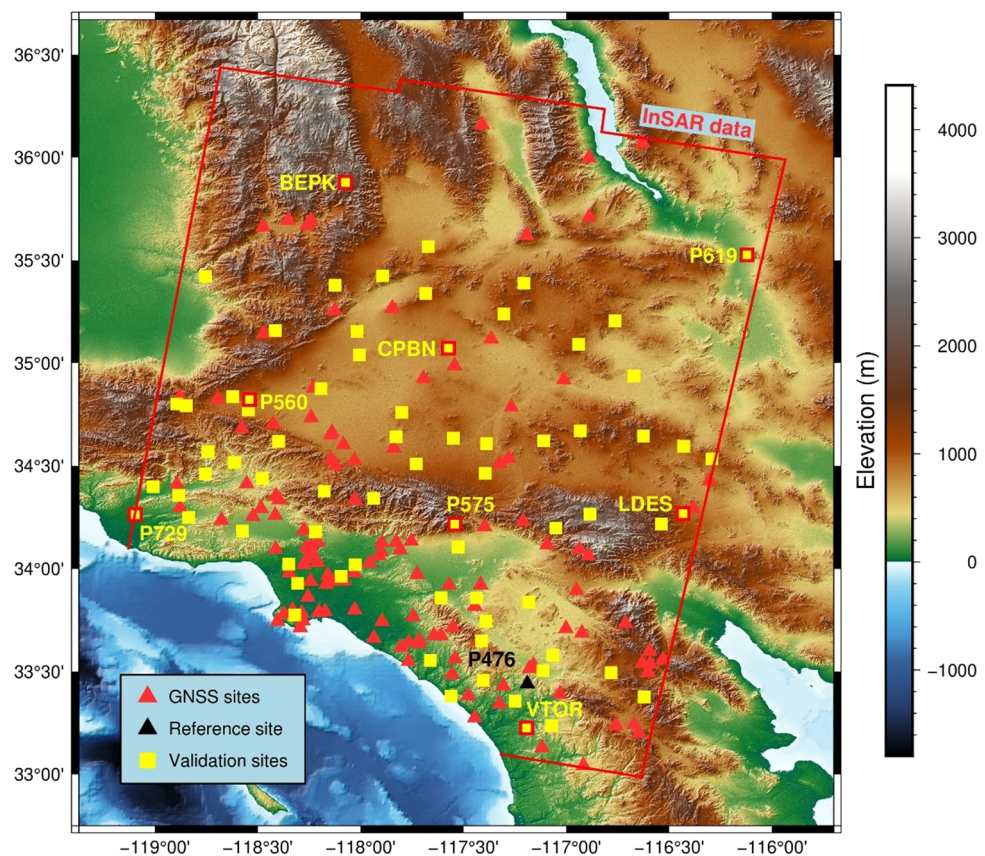


**Fig. 6** Model validation results and original LOS direction displacements of 5 periods InSAR data in the San Francisco Bay Area. The first column represents the original InSAR displacement, the second column represents the model validation result, the third column shows the residual of the model validation result, and the fourth column is the

histogram of residual distribution (since most of the residual values are between -20 and 20 mm, the plotting range of the histogram is set to -20 to 20 mm to facilitate display). The color bar on the left corresponds to the figures in the first and second columns, and the color bar on the right corresponds to the figures in the third column

**Fig. 7** Spatial distribution of topography and GNSS sites in Southern California. The red solid line is the InSAR data footprint. The squares and triangles denote GNSS site locations, squares represent the site used for Jackknife cross-validation, those with red frame show the results in the paper, and the others show the results in the Supplementary Material



from the Nevada Geodesy Laboratory (Blewitt et al. 2018), and 199 sites were selected.

We select P476 as the reference site to unify the measurement geometry in the same way as above, and row “a” of Fig. 8 shows 5 periods of InSAR displacement time series data at equal intervals after unified measurement geometry. The results of all 72 periods (considering the picture layout and the displacement of the first period is the reference zero value, we ignore the data of the first period when plotting) are shown in Fig. S16a and Fig. S16b, the displacement comparison of the GNSS sites and adjacent InSAR pixel is shown in Fig. S17 in the Supplementary Material.

As can be seen in row “a” of Fig. 8, Fig. S16a and S16b, the overall deformation mode is mainly manifested as subsidence, with the highest magnitude in the southwest part and a relatively gentle deformation trend in the northern region. The trend item was removed in the same way as described above (Fig. S18 in the Supplementary Material).

### 3.2.2 InSAR data spatial modeling

We adopted the method introduced in Sect. 2.2.1 to select spatial bases (Fig. S19 in the Supplementary Material), and the three selected range values were  $0.856^\circ$ ,  $0.428^\circ$ , and  $0.214^\circ$  and the basis numbers were 16, 55, and 220. The specific

spatial basis distribution is shown in Fig. S20 in the Supplementary Material.

After the spatial basis was determined, the time-varying state arguments were obtained by least squares as described in Eq. (5), and 5 periods InSAR data spatial modeling results and residuals are shown in row “b” and row “d” of Fig. 8, all 72 periods InSAR data spatial modeling results and residuals are shown in Fig. S21a, S21b and Fig. S22a, S22b in the Supplementary Material. The error RMS value of the spatial modeling is shown in Fig. S23.

As shown in row “b” of Fig. 8, Fig. S21a and S21b, the overall deformation trend can be obtained through the spatial model, but the deformation information is too smooth, and some obvious deformation details are omitted. This means that the spatial model can obtain the overall deformation potential, but as time progresses, the model cannot fully capture the deformation changes. Fig. S22a and S22b show that the spatial modeling error is small in most areas, but the error is large in some areas and the value even exceeds 20 mm. Fig. S23 shows that the error RMS value is distributed in the range of 2–7 mm, and gradually increases over time, which means that the deviation between the modeling results and the InSAR displacement increases gradually, and the spatial model cannot fully reflect the temporal evolution of displacement.

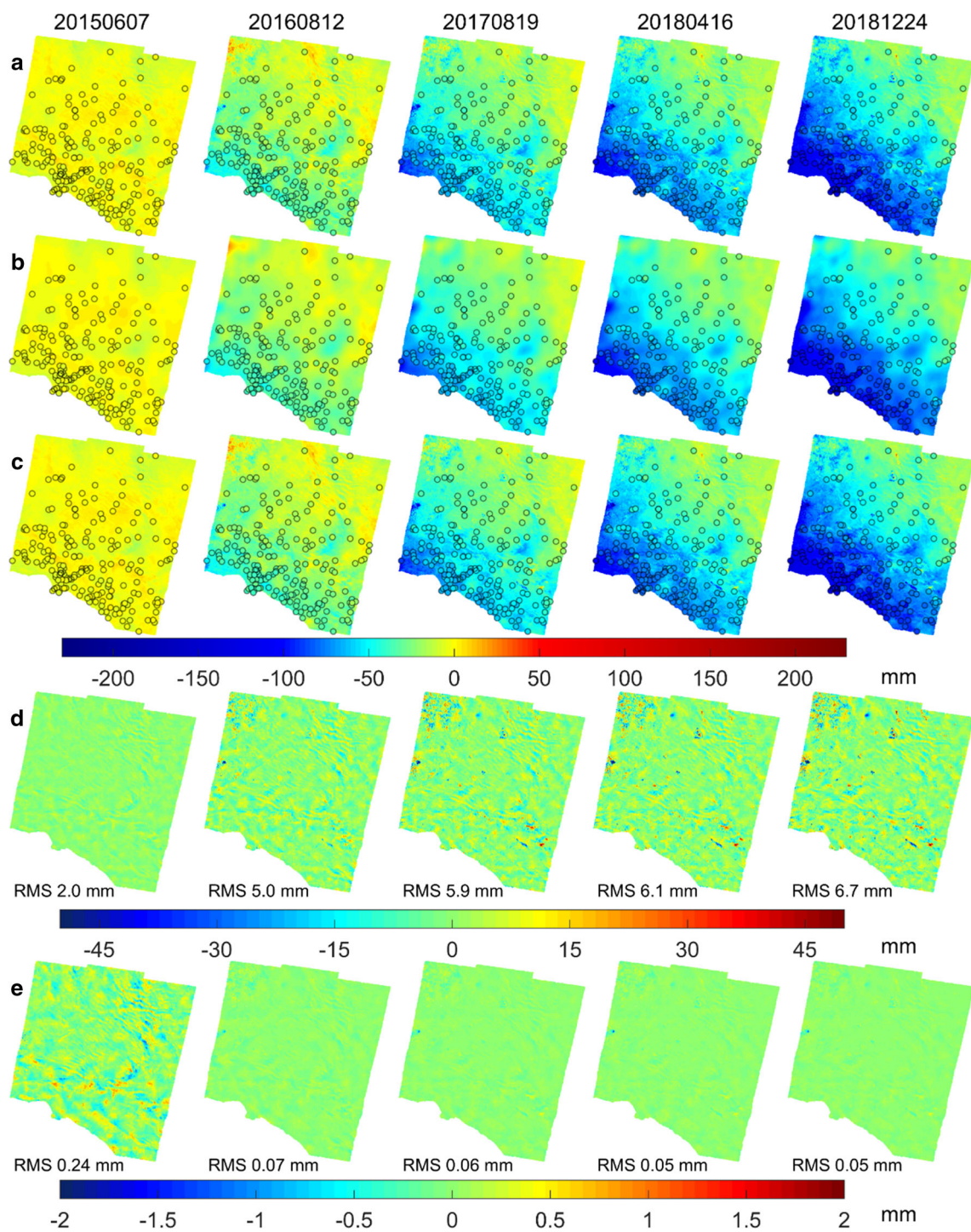


**Fig. 8** Combination diagram of 5 periods InSAR displacement time series data relative to 2015-05-14 in Southern California. The rows "a", "b" and "c" respectively represent the InSAR data after measurement geometry unified, spatial modeling results and fusion results, the circle indicates the GNSS site locations, and the color indicates the deformation value. The row "d" represents the residual of spatial modeling,

and row "e" represents the residual of the fusion result. Warm colors (i.e., positive values) denote surface displacements toward the satellite, and cold colors (i.e., negative values) denote the away-motion from the satellite

### 3.2.3 GNSS and InSAR data fusion

The GNSS data were added to the data fusion process, and we selected all the sites that had data throughout the whole InSAR measurement period (a total of 74 sites) to test the accuracy of the improved STRE model. The comparison results of 8 sites are shown in Fig. 9, and the other 66 sites are shown in Fig. S24a and S24b of the Supplementary Material.

For the InSAR fusion result, we show the improved STRE model displacement results (row “c” of Fig. 8) and residual (row “e” of Fig. 8) of 5 periods InSAR data, and all 72 periods results and residual are shown in Fig. S25a, S25b and Fig. S26a, S26b of the Supplementary Material.

Figure 9, Fig. S24a and S24b show that the model results of the improved STRE model are in good agreement with the GNSS displacement, which accurately reflect the overall displacement trend and the value changes, and the stability of the model results relative to the GNSS displacement data has also been further strengthened. Except for the P561 site, the error RMS values are all less than 5 mm. At site P561, the larger error RMS is a result of fluctuations in the GNSS observation data while the improved STRE model is relatively stable.

As shown in row “c” of Fig. 8, Fig. S25a and S25b, after adding the GNSS data for EM estimation, the model results are more consistent with the InSAR deformation data and capture more deformation information based on the spatial model, especially in the southwest part.

Row “e” of Fig. 8, Fig. S23, S26a and S26b show that there is no obvious deformation information missing of the improved STRE model, and the error distribution is basically random, with the error RMS value less than 0.25 mm. Furthermore, the RMS value showed a gradually decreasing trend, it gradually stabilized and eventually dropped to approximately 0.05 mm. These indicate that the improved STRE model has good stability and reliability in spatial and temporal domain, while enriching the observation data, the time-varying information and subtle variation are more and more fully captured, and the fusion result is gradually approaching the InSAR displacement observation data.

Based on the fusion results, the CSBAS method (Neely et al. 2019) was used to calculate the deformation rate field as shown in Fig. 10.

Figure 10 (left) shows that the displacement rates on both sides of the fault are significantly different, and the deformation can be roughly divided into three parts along the line from northeast to southwest, which is consistent with results from Hearn (2019). The rate of the first part was relatively small and uniform, concentrated from 0 to  $-10$  mm/yr, which is basically the same as the Panamint Valley fault and Death Valley fault calculated by other scholars (Johnson 2013; Zeng and Shen 2014, 2016). The rate of the second part was approximately  $-10$  to  $-20$  mm/yr, the southwest

direction was slightly larger, and the deformation rate of the Garlock fault in the area was in good agreement with results from Hearn (2019). Areas with large subsidence rates were mainly distributed in the third part of the southwest corner, some of which were close to  $-35$  mm/yr, and the San Andreas Fault (Mojave, Bernardino, Jacinto, and Gorgonio) deformation rate was equivalent to that of Johnson (2013) and Evans (2018).

In addition, some deformation anomalies in the displacement velocity figure correspond well to areas of known anthropogenic activities. For the local deformation anomaly area northwest of point 2, the Corso volcanic field is on the west side of this anomaly area, and there is one of the largest geothermal generators in the United States located in this deformation anomaly area ("<https://www.usgs.gov/volcanoes/coso-volcanic-field>"). For the local deformation anomaly area east of point 2, Sears Lake is located at this location, due to a huge resource of sodium and potassium minerals of the carbonate, sulfate, borate and halide classes of mineralogy, the mining activities here are very active ("[https://en.wikipedia.org/wiki/Searles\\_Lake](https://en.wikipedia.org/wiki/Searles_Lake)").

Figure 10 (right) shows that the fusion results are in good agreement with the InSAR displacement, which can provide deformation data with higher time resolution, and the error RMS value less than 0.7 mm. This means that within the time interval of InSAR observations, the fusion results can provide effective deformation results, enabling us to grasp high-temporal dynamic deformation information and better understand deformation evolution, which can compensate for the low spatial resolution of GNSS and the low temporal resolution of InSAR data.

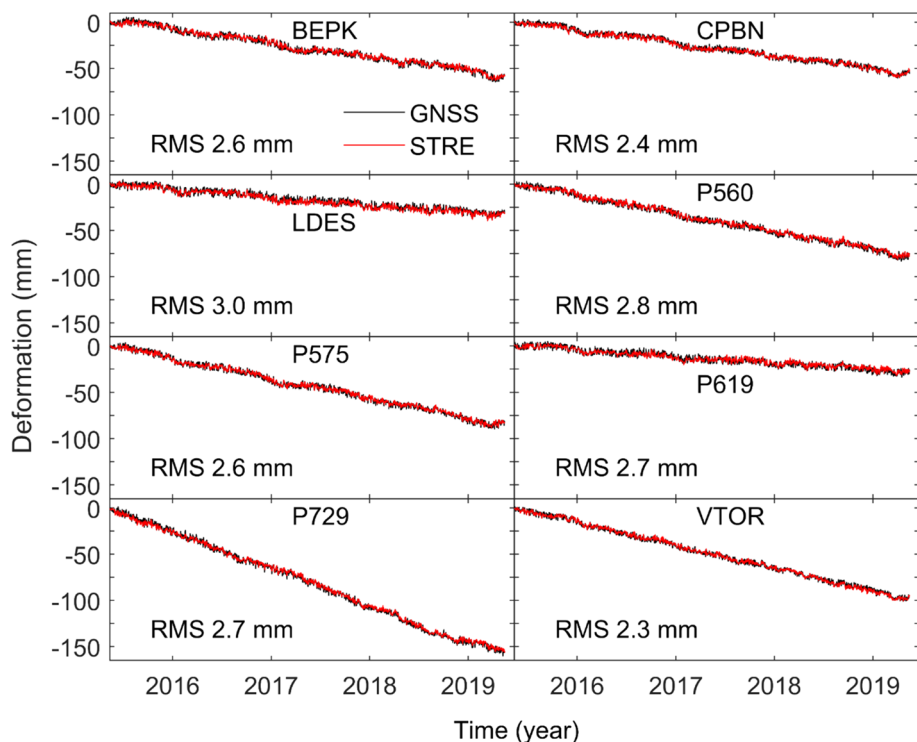
### 3.2.4 Jackknife cross-validation

We verified the accuracy and external reliability of the improved STRE model using Jackknife cross-validation. 8 GNSS sites (Fig. 11) and 6 periods InSAR data with the same interval (Fig. 12) are used for display. The validation results of other 66 GNSS sites are shown in Fig. S27a and S27b, the validation results and residuals of all 72 periods data are shown in Fig. S28a, S28b, S29a and S29b, the error RMS values are listed in Table S4 of the Supplementary Material.

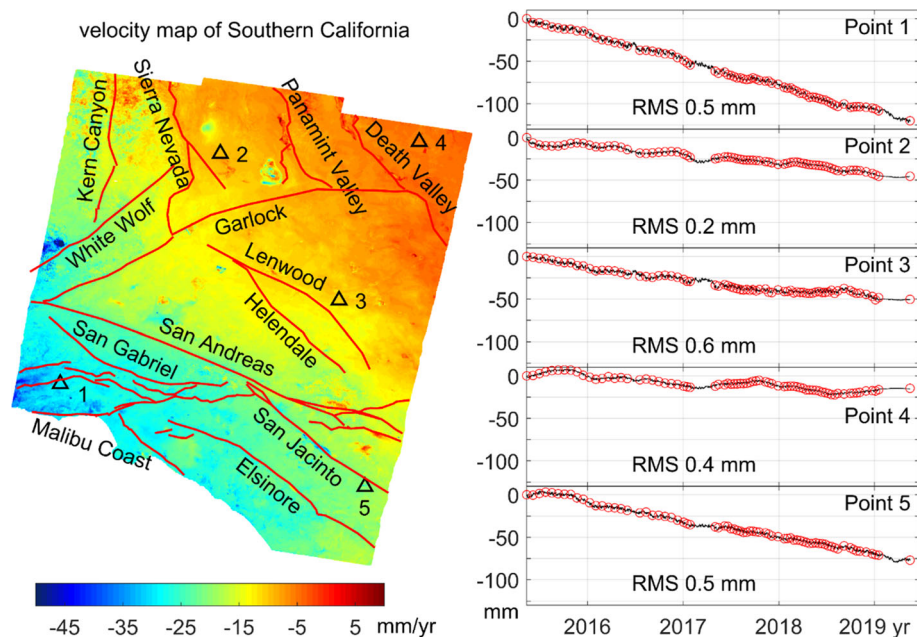
As can be seen from Fig. 11, Fig. S27a and S27b, the results of Jackknife cross-validation are basically consistent with the original GNSS displacement. Most of the error RMS values are less than 6 mm, except for the OPRD site, where the RMS values are all less than 10 mm. In general, although the validation results show a little fluctuation and deviation, they can properly reflect the GNSS displacement trend and deformation magnitude.

Figure 12, Fig. S28a and S28b show that the validation results can reflect the original InSAR displacement information, although there is some deformation information that

**Fig. 9** Model fusion results and original displacements in the LOS direction of 8 GNSS sites in Southern California. The red line is the result of the improved STRE model, the black line is the original GNSS displacement in the LOS direction



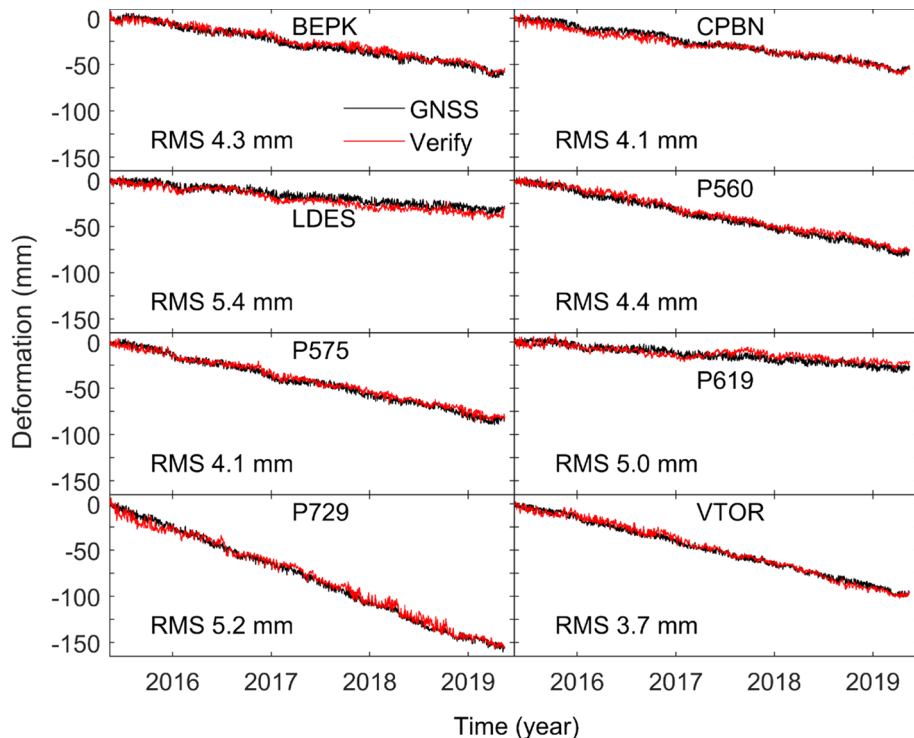
**Fig. 10** The deformation rate field in the LOS direction of Southern California and the fusion results of 5 representative pixels. The figures on the left shows the deformation rate field in the LOS direction, the triangles represent the location of the InSAR pixel shown on the right, and the solid red lines indicate the locations of several major faults (Styron and Pagani 2020). For the figures on the right, the black line represents the fusion result, and the circles represent the InSAR displacement value



cannot be fully reflected, this may be the atmospheric delay missed by the fusion model. Since the InSAR data corresponding to the modeling period does not participate in the validation process, we only use the InSAR data before and after this period and GNSS data for modeling, and the spatial distributions of GNSS sites are relatively sparse compared to the InSAR resolution, which leads the fusion model unable to fully capture the deformation caused by the regional water

vapor phase delay. The validation results residual distribution map (Fig. S29a and S29b) show that this part of the error is clustered and random in spatial domain, most values are less than 5 mm, which did not affect the expression of the displacement by the fusion model. The residual error histogram (the fourth column of Fig. 12) shows that the residuals are concentrated within 2 mm and the error distributions are close to a normal distribution, which further proves the stability and reliability of the improved STRE model.

**Fig. 11** Jackknife cross-validation results and original displacements in the LOS direction of 8 GNSS sites in Southern California. The red line is the result of Jackknife cross-validation, the black line is the original GNSS displacement in the LOS direction



From Table S4, we can see that the error RMS value is mostly around 2 mm. As for the San Francisco Bay Area example, the last period of data reveals a higher error RMS since the model cannot obtain deformation information from subsequent observation periods. Except for the last period (2019-05-17) where the error RMS value is greater than 4 mm, the RMS values are all less than 3 mm. This proves that the improved STRE model has good reliability and stability in spatial and temporal domain. Even if there is no original InSAR deformation data to supplement, the improved STRE model can correctly predict the InSAR displacement value and its deformation potential, and the results are basically consistent with the original InSAR displacement data.

## 4 Conclusions

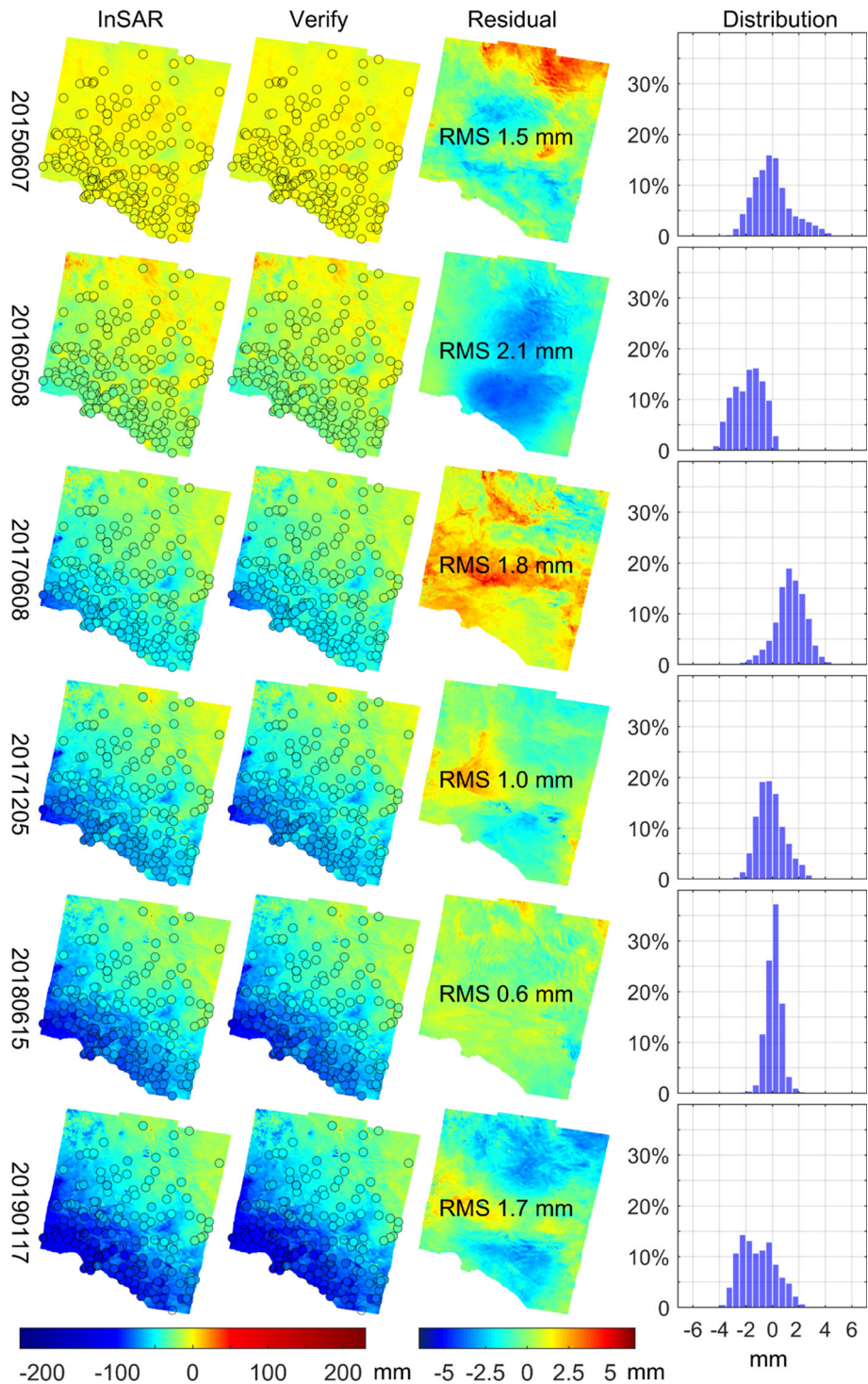
GNSS and InSAR data fusion can give full play to the advantages of these two geodetic methods, and the STRE model has a high potential for reliable data fusion. However, it has the limitations of relying on prior information and lacks experimental confirmation. To solve these two problems, we proposed a spatial basis automatic selection method to improve the STRE model and applied it to the fusion of GNSS and InSAR deformation data in the San Francisco Bay Area and Southern California. For these two experiments, the improved STRE model showed excellent data fusion effects and no longer depended on prior information

and personal experience, significantly enhancing the adaptability of the model. Regarding the problem of insufficient GNSS and InSAR data in deformation monitoring and disaster awareness, the improved STRE model is expected to play an important role in providing high spatio-temporal resolution and high-precision deformation result.

The results of spatial modeling using InSAR data show that spatial modeling can obtain the overall deformation trend of the study area, and has a good ability to capture large-scale deformation signals. For the two experiments, most of the spatial modeling residuals are less than 15 mm, and as the study area increases, the number of selected spatial bases increases from 149 to 291, which means that the calculation of the model does not increase significantly. However, for some small-scale subtle deformation, spatial modeling is difficult to capture, resulting in too smooth results and the model residual presents a gradually increasing trend.

After adding GNSS data for fusion, the residual error of the previous spatial model is greatly improved, especially in areas with complex deformation conditions. In terms of the error of the fusion results, most of the model errors are less than 3 mm, and the InSAR error RMS value of each period is less than 0.3 mm, indicating that with the enrichment of displacement data, time-varying information and subtle variation are increasingly fully captured, the fusion results gradually approach the observed displacement values, which proves that the improved STRE model has good stability and reliability in the time domain. More importantly, in the InSAR data gap, the improved STRE model can interpolate

**Fig. 12** Model validation results and original LOS direction displacements of 6 periods InSAR data in Southern California. The first column represents the original InSAR displacement, the second column represents the model validation result, the third column shows the residual of the model validation result, and the fourth column is the histogram of residual distribution. The color bar on the left corresponds to the figures in the first and second columns, and the color bar on the right corresponds to the figures in the third column



the continuous displacement time series with high temporal resolution and high precision, which compensates for the deficiency in GNSS low spatial resolution and InSAR low temporal resolution.

Using the fusion results of the improved STRE model to calculate the deformation rate field, it is found that our calculation results can accurately reflect the difference in

deformation rates on both sides of a fault, and the deformation rate and its spatial distribution are in good agreement with the research results of other scholars for the two areas of interest (San Francisco Bay and Southern California). For some abnormal deformation areas detected in the rate field, the deformation corresponds well with the location of known anthropogenic activities. All these indicate that the improved

model is suitable for fusing a large amount of long-term GNSS and InSAR data, and it can play an important role in providing high spatio-temporal resolution and high-precision deformation data, to help us obtain more detailed deformation evolution information.

The Jackknife cross-validation results further demonstrate that the improved STRE model has good spatial and temporal stability and reliability. For the GNSS validation results, the model results can correctly capture the observed displacement information, and the model results agree well with the original GNSS displacement. Although the model results are sometimes overestimating or underestimating the observed deformation, the frequency of this abnormal situation is low, and the error RMS values are mostly less than 8 mm. For the InSAR validation results, the model can properly reflect the overall deformation behavior, but some local deformation information will still be missed. Fortunately, the spatial distribution of the residual is relatively random, the residual values are close to a normal distribution and most of the errors are within 10 mm.

Our current research mainly focuses on the deformation in the LOS direction. In the future, we intend to conduct more in-depth research on fusing multi-geometry InSAR data with GNSS data to recover the high-precision three-dimensional deformation field. Furthermore, combining the selection of spatial bases with the down-sampling algorithm is also our next research plan, which is expected to further improve the stability and reliability of the model.

**Supplementary Information** The online version contains supplementary material available at <https://doi.org/10.1007/s00190-022-01636-7>.

**Acknowledgements** The authors thank Peiliang Xu, the Assistant Editor-in-Chief and two anonymous reviewer for their constructive comments that helped improve the manuscript. This work was funded by the National Key R&D Program of China (2019YFC1509205), the National Natural Science Foundation of China (No. 42174023), the National Natural Science Foundation of China (No. 42174053), the Natural Science Foundation of Hunan Province, China (No. 2021JJ30805), the Fundamental Research Funds for the Central Universities of Central South University (No. 2020zzts175) and the Postgraduate Scientific Research Innovation Project of Hunan Province (No. CX20200231). We would like to thank the ARIA for providing the Sentinel-1A/B standardized interference products and MintPy software, thank the Nevada Geodesy Laboratory for providing the GNSS data. We would also like to thank Neely for his help on the CSBAS method and Xiaohua Xu for providing the InSAR time series data of Southern California. Maps and plots in the paper were made using the Generic Mapping Tools and MATLAB.

**Author's contributions** WD and WX provided the initial idea and designed the experiments for this study; HY carried out the designed experiments and wrote the paper; LX processed and analyzed the InSAR data of the San Francisco Bay Area; WD and WX contributed to the final manuscript with suggestions and corrections.

**Availability of data and material** The Sentinel-1A/B standardized interference products of the San Francisco Bay Area are available in the

ARIA, <https://aria.jpl.nasa.gov/products>. The InSAR time series of Southern California are provided by Xiaohua Xu, <https://topex.ucsd.edu/gmtsar/insargen/>. The GNSS data is obtained from the Nevada Geodesy Laboratory, <http://geodesy.unr.edu>.

## References

- Aslan G, Lasserre C, Cakir Z et al (2019) Shallow creep along the 1999 Izmit Earthquake rupture (Turkey) from GPS and high temporal resolution interferometric synthetic aperture radar data (2011–2017). *J Geophys Res: Solid Earth* 124:2218–2236
- Bekaert D, Segall P, Wright TJ, Hooper AJ (2016) A network inversion filter combining GNSS and InSAR for tectonic slip modeling. *J Geophys Res: Solid Earth* 121:2069–2086. <https://doi.org/10.1002/2015JB012638>
- Blewitt G, Hammond WC, Kreemer C (2018) Harnessing the GPS data explosion for interdisciplinary science. *Eos*. <https://doi.org/10.1029/2018EO104623>
- Bürgmann R, Hilsley G, Ferretti A, Novali F (2006) Resolving vertical tectonics in the San Francisco Bay Area from permanent scatterer InSAR and GPS analysis. *Geology* 34:221–224. <https://doi.org/10.1130/G22064.1>
- Cao Y, Li Z, Wei J et al (2018) Stochastic modeling for time series InSAR: with emphasis on atmospheric effects. *J Geodesy* 92:185–204. <https://doi.org/10.1007/s00190-017-1055-5>
- Carlà T, Tofani V, Lombardi L et al (2019) Combination of GNSS, satellite InSAR, and GBInSAR remote sensing monitoring to improve the understanding of a large landslide in high alpine environment. *Geomorphology* 335:62–75. <https://doi.org/10.1016/j.geomorph.2019.03.014>
- Chaussard E, Bürgmann R, Shirzaei M et al (2014) Predictability of hydraulic head changes and characterization of aquifer-system and fault properties from InSAR-derived ground deformation. *J Geophys Res: Solid Earth* 119:6572–6590. <https://doi.org/10.1002/2014JB011266>
- Cressie N (1990) The origins of kriging. *Mathem Geol* 22:239–252. <https://doi.org/10.1007/BF00889887>
- Cressie N, Johannesson G (2008) Fixed rank kriging for very large spatial data sets. *J Royal Stat Soc: Series B (statistical Methodology)* 70:209–226. <https://doi.org/10.1111/j.1467-9868.2007.00633.x>
- Cressie N, Shi T, Kang EL (2010) Fixed rank filtering for spatio-temporal data. *J Comput Graph Stat* 19:724–745. <https://doi.org/10.1198/jcgs.2010.09051>
- Evans EL (2018) A comprehensive analysis of geodetic slip-rate estimates and uncertainties in CaliforniaA comprehensive analysis of geodetic slip-rate estimates and uncertainties in California. *Bull Seismol Soc Am* 108:1–18. <https://doi.org/10.1785/0120170159>
- Farolfi G, Bianchini S, Casagli N (2018) Integration of GNSS and satellite InSAR data: derivation of fine-scale vertical surface motion maps of Po Plain, Northern Apennines, and Southern Alps, Italy. *IEEE Trans Geosci Remote Sens* 57:319–328. <https://doi.org/10.1109/TGRS.2018.2854371>
- Fattah H, Amelung F (2013) DEM error correction in InSAR time series. *IEEE Trans Geosci Remote Sens* 51:4249–4259. <https://doi.org/10.1109/TGRS.2012.2227761>
- Fialko Y, Simons M, Agnew D (2001) The complete (3-D) surface displacement field in the epicentral area of the 1999 Mw7. 1 Hector Mine earthquake, California, from space geodetic observations. *Geophys Res Lett* 28:3063–3066. <https://doi.org/10.1029/2001GL013174>
- Field EH, Arrowsmith RJ, Biasi GP et al (2014) Uniform California earthquake rupture forecast, version 3 (UCERF3)—the time-independent model. *Bull Seismol Soc Am* 104:1122–1180. <https://doi.org/10.1785/0120130164>

- Field EH, Biasi GP, Bird P et al (2015) Long-term time-dependent probabilities for the third uniform California earthquake rupture forecast (UCERF3). *Bull Seismol Soc Am* 105:511–543. <https://doi.org/10.1785/0120140093>
- Fuhrmann T, Garthwaite MC (2019) Resolving three-dimensional surface motion with InSAR: Constraints from multi-geometry data fusion. *Remote Sensing* 11:241. <https://doi.org/10.3390/rs11030241>
- Fuhrmann T, Caro Cuenca M, Knöpfler A et al (2015) Estimation of small surface displacements in the upper rhine graben area from a combined analysis of PS-InSAR, levelling and GNSS data. *Geophys J Int* 203:614–631. <https://doi.org/10.1093/gji/ggv328>
- Fukuda J, Johnson KM (2010) Mixed linear—non-linear inversion of crustal deformation data: Bayesian inference of model, weighting and regularization parameters. *Geophys J Int* 181:1441–1458. <https://doi.org/10.1111/j.1365-246X.2010.04564.x>
- Harville DA (1977) Maximum likelihood approaches to variance component estimation and to related problems. *J Am Stat Assoc* 72:320–338. <https://doi.org/10.1080/01621459.1977.10480998>
- Hearn EH (2019) Kinematics of southern California crustal deformation: Insights from finite-element models. *Tectonophysics* 758:12–28. <https://doi.org/10.1016/j.tecto.2019.02.016>
- Hu J, Zhu JJ, Li ZW, et al (2011) Robust Estimating Three-Dimensional Ground Motions from Fusion of InSAR and GPS Measurements. In: 2011 International Symposium on Image and Data Fusion. pp 1–4
- Ji P, Lv X, Dou F, Yun Y (2020) Fusion of GPS and InSAR data to derive robust 3D deformation maps based on MRF L1-regularization. *Remote Sens Lett* 11:204–213. <https://doi.org/10.1080/2150704X.2019.1701722>
- Johnson K (2013) Slip rates and off-fault deformation in Southern California inferred from GPS data and models. *J Geophys Res: Solid Earth* 118:5643–5664. <https://doi.org/10.1002/jgrb.50365>
- Johnston P, Filmer M, Fuhrmann T (2021) Evaluation of methods for connecting InSAR to a terrestrial reference frame in the Latrobe Valley, Australia. *J Geodesy* 95:1–18. <https://doi.org/10.1007/s00190-021-01560-2>
- Jolivet R, Grandin R, Lasserre C et al (2011) Systematic InSAR tropospheric phase delay corrections from global meteorological reanalysis data. *Geophys Res Lett*. <https://doi.org/10.1029/2011GL048757>
- Jolivet R, Agram PS, Lin NY et al (2014) Improving InSAR geodesy using global atmospheric models. *J Geophys Res: Solid Earth* 119:2324–2341. <https://doi.org/10.1002/2013JB010588>
- Katzfuss M, Cressie N (2011) Spatio-temporal smoothing and EM estimation for massive remote-sensing data sets. *J Time Ser Anal* 32:430–446. <https://doi.org/10.1111/j.1467-9892.2011.00732.x>
- Kooi H, De Vries J (1998) Land subsidence and hydrodynamic compaction of sedimentary basins. *Hydrol Earth Syst Sci* 2:159–171. <https://doi.org/10.5194/hess-2-159-1998>
- Liu N, Dai W, Santerre R et al (2018) High spatio-temporal resolution deformation time series with the fusion of InSAR and GNSS data using spatio-temporal random effect model. *IEEE Trans Geosci Remote Sens* 57:364–380. <https://doi.org/10.1109/TGRS.2018.2854736>
- Mahapatra P, van der Marel H, van Leijen F et al (2018) InSAR datum connection using GNSS-augmented radar transponders. *J Geodesy* 92:21–32. <https://doi.org/10.1007/s00190-017-1041-y>
- Miller RG (1974) The jackknife—a review. *Biometrika* 61:1–15. <https://doi.org/10.1093/biomet/61.1.1>
- Minson SE, Murray JR, Langbein JO, Gomberg JS (2014) Real-time inversions for finite fault slip models and rupture geometry based on high-rate GPS data. *J Geophys Res: Solid Earth* 119:3201–3231. <https://doi.org/10.1002/2013JB010622>
- Neely WR, Borsa AA, Silverii F (2019) GInSAR: A cGPS correction for enhanced InSAR time series. *IEEE Trans Geosci Remote Sens* 58:136–146. <https://doi.org/10.1109/TGRS.2019.2934118>
- Shi Q, Dai W, Santerre R et al (2019) Spatially heterogeneous land surface deformation data fusion method based on an enhanced spatio-temporal random effect model. *Remote Sens* 11:1084. <https://doi.org/10.3390/rs11091084>
- Shirzaei M, Bürgmann R (2018) Global climate change and local land subsidence exacerbate inundation risk to the San Francisco Bay Area. *Sci Adv* 4:9234. <https://doi.org/10.1126/sciadv.aap9234>
- Shumway RH, Stoffer DS (1982) An approach to time series smoothing and forecasting using the EM algorithm. *J Time Ser Anal* 3:253–264
- Styron R, Pagani M (2020) The GEM global active faults database. *Earthq Spectra* 36:160–180. <https://doi.org/10.1177/8755293020944182>
- Walters R, Parsons B, Wright T (2014) Constraining crustal velocity fields with InSAR for Eastern Turkey: limits to the block-like behavior of Eastern Anatolia. *J Geophys Res: Solid Earth* 119:5215–5234. <https://doi.org/10.1002/2013JB010909>
- Wan YG, Shen ZK, R.Bürgmann, et al (2018) Fault geometry and slip distribution of the 2008 MW7.9 Wenchuan, China earthquake, inferred from GPS and InSAR measurements. *Reviews of Geophysics and Planetary Physics* 49:27
- Xiao R, Yu C, Li Z, He X (2021) Statistical assessment metrics for InSAR atmospheric correction: Applications to generic atmospheric correction online service for InSAR (GACOS) in Eastern China. *Int J Appl Earth Obs Geoinf* 96:102289. <https://doi.org/10.1016/j.jag.2020.102289>
- Xu P, Liu Y, Shen Y, Fukuda Y (2007) Estimability analysis of variance and covariance components. *J Geodesy* 81:593–602
- Xu C, Gong Z, Niu J (2016) Recent developments in seismological geodesy. *Geodesy and Geodyn* 7:157–164
- Xu X, Sandwell DT, Tymofeyeva E et al (2017) Tectonic and anthropogenic deformation at the Cerro Prieto geothermal step-over revealed by Sentinel-1A InSAR. *IEEE Trans Geosci Remote Sens* 55:5284–5292. <https://doi.org/10.1109/TGRS.2017.2704593>
- Xu W, Wu S, Materna K et al (2018) Interseismic ground deformation and fault slip rates in the greater San Francisco Bay Area from two decades of space geodetic data. *J Geophys Res: Solid Earth* 123:8095–8109. <https://doi.org/10.1029/2018JB016004>
- Xu X, Sandwell DT, Klein E, Bock Y (2021) Integrated sentinel-1 InSAR and GNSS time-series along the San Andreas fault system. *J Geophys Res: Solid Earth*. <https://doi.org/10.1029/2021JB022579>
- Yu C, Li Z, Penna NT (2020) Triggered afterslip on the southern Hikurangi subduction interface following the 2016 Kaikōura earthquake from InSAR time series with atmospheric corrections. *Remote Sens Environ* 251:112097. <https://doi.org/10.1016/j.rse.2020.112097>
- Zeng Y, Shen Z-K (2014) Fault network modeling of crustal deformation in California constrained using GPS and geologic observations. *Tectonophysics* 612:1–17. <https://doi.org/10.1016/j.tecto.2013.11.030>
- Zeng Y, Shen Z-K (2016) A fault-based model for crustal deformation, fault slip rates, and off-fault strain rate in California. *Bull Seismol Soc Am* 106:766–784. <https://doi.org/10.1785/0120140250>
- Zhang Y, Fattah H, Amelung F (2019) Small baseline InSAR time series analysis: unwrapping error correction and noise reduction. *Comput Geosci* 133:104331. <https://doi.org/10.1016/j.cageo.2019.104331>